Effect of Bed Clay on Surface Water-Wave Reconstruction from Ripples

Jonathan Malarkey[1*], Ellen M. Pollard[2], Roberto Fernández[3], Xuxu Wu[2,4], Jaco H. Baas[1] and Daniel R. Parsons[5]

[1]School of Ocean Sciences, Bangor University, Menai Bridge, Anglesey LL59 5AB, UK.
[2]Energy and Environment Institute, University of Hull, Hull, HU6 7RX, UK.
[3]Department of Civil and Environmental Engineering, The Pennsylvania State University, State College, PA 16802, USA.
[4]School of Environmental Sciences, University of Hull, Hull, HU6 7RX, UK.
[5]Department of Geography and Environment, Loughborough University, Loughborough, LE11 3TU, UK.

[*]Corresponding author: Jonathan Malarkey (j.malarkey@bangor.ac.uk)

Abstract

Wave ripples can provide valuable information on their formative hydrodynamic conditions in past subaqueous environments by inverting dimension predictors. However, these inversions do not usually take the mixed non-cohesive/cohesive nature of sediment beds into account. Recent experiments involving sand–kaolinite mixtures have demonstrated that wave-ripple dimensions and the threshold of motion are affected by bed clay content. Here, a clean-sand method to determine wave climate from orbital ripple wavelength has been adapted to include the effect of clay and a consistent shear-stress threshold parameterisation. From present-day examples with known wave conditions, the results show that the largest clay effect occurs for coarse sand with median grain diameters over 0.45 mm. For a 7.4% volumetric clay concentration, the range of possible water-surface wavelengths and water depths can be reduced significantly, by factors of three and four compared to clean sand, indicating that neglecting clay when present will underestimate the wave climate.

Introduction

Bed-surface structures in sediments and sedimentary rocks of past subaqueous environments provide important information on flow hydraulics[1]. These structures tend to be classified on the basis of the presence or absence of cohesion in equivalent modern environments: (a) cohesive structures, associated with physical cohesion by clay particles and biological cohesion by extracellular polymeric substances (e.g. biofilms[2]), where the bed is stabilised by cohesion between grains and sudden catastrophic failure may occur under high bed shear stress, e.g. during storms; and (b) non-cohesive bedforms (e.g. wave and current ripples[3,4]), where grains can move individually and tend to respond more rapidly and continuously to changes in flow forcing[5]. Examples of these types of bed-surface structure include roll-ups[6] and non-cohesive wave ripples[7]. Davies et al.[8] argued that the distinction between cohesive and non-cohesive sedimentary structures is artificial, as they represent end members of a spectrum, and thus predictions based on one classification may result in misinterpretations. This position is re-enforced by recent experiments that have shown how sandy bedforms can be affected by small amounts of biological and physical cohesion[9,10,11,12]. The consequence for wave ripples of physical cohesion associated with kaolin clay in the bed has been detailed by Wu et al.[13]. Building on previous work[7], Diem[14] developed a clean-sand analytical method for the prediction of paleowave climate based on the dimensional measurement of wave ripples in the rock record[15,16,17,18,19]. Here, the Diem[14] approach is adapted for sand–clay mixtures, using the synthesis proposed by Wu et al.[13].

The Diem[14] approach starts by determining the wave orbital diameter from the ripple wavelength, without requiring a specific wavelength predictor. Here, the formulation starts as Diem[14] did, with linear wave theory and additional constraints based on threshold of motion and wave breaking. It will then return to the effect of clay on ripple-wavelength prediction and the threshold of motion. Since wave conditions from the rock record are unknow, the importance of clay content is demonstrated with the use of present-day examples from the laboratory and field, where the wave conditions were known.

Results

The Diem[14] approach

Wave conditions

Based on linear wave theory, the Diem[14] approach uses expressions for the dispersion relation and the wave-velocity amplitude, U_0, together with conditions for the threshold of motion and wave breaking, to give

$$x < \tanh kh, \quad x \geq A\cosh kh, \tag{1a,b}$$

(see methods) where $x = L/L_{t\infty}$, L is the water-surface wavelength, $L_{t\infty} = \frac{1}{2}\pi g(d_0/U_t)^2$ is the deep-water surface wavelength corresponding to the threshold of motion, $k = 2\pi/L$, h is the water depth, g is the acceleration due to gravity (= 9.81 m s^{-2}), d_0 is the orbital diameter (= H/sinhkh, H is the wave height), U_t is the critical wave-velocity amplitude associated with the threshold of motion and $A = d_0/0.142L_{t\infty}$. As will be seen later, U_t is a function of d_0 and D_{50}, the median grain diameter, and A can be defined as $\frac{1}{2}(U_t/U_m)^2$, where $U_m = (0.0355\pi g d_0)^{1/2}$ is the maximum wave-velocity amplitude. Since wave-velocity amplitude and orbital diameter are related by $U_0 = \pi d_0/T$, where T is the wave period, U_0 and T are in the ranges $U_t < U_0 \leq U_m$ and $\pi d_0/U_m \leq T < \pi d_0/U_t$.

Eqs. (1a,b) represent the range of possible conditions between threshold and wave breaking for the wave climate, such that x is in the range $A\cosh kh \leq x < \tanh kh$, and $A < \frac{1}{2}$ for there to be any allowable conditions (see methods). Figure 1 shows kh versus x for the limiting single-valued $A = \frac{1}{2}$ case ($U_m^2 = U_t^2$) from shallow water ($kh \ll 1$) to deep water ($kh \gg 1$). Figure 1 also shows the $A = \frac{1}{4}$ case ($U_m^2 = 2U_t^2$), corresponding to typical above-threshold wave conditions. In the latter case, the shaded region in Figure 1 shows the allowable values of x [the methods section explains how intersection points, (x_{min}, kh_{min}) and (x_{max}, kh_{max}), are determined]. The breaking-wave curves ($x = A\cosh kh$) are concave downward and the threshold curve ($x = \tanh kh$) is concave upward. Notice for the breaking-wave curves, $x \rightarrow A$ for $kh \ll 1$ and A also controls the slope for larger kh. In dimensional terms, L is

therefore limited by the threshold scale ($L_{t\infty}$) and breaking-wave scale ($AL_{t\infty}$) according to $AL_{t\infty} < L \leq L_{t\infty}$. Then, from eqs. (1a,b), the range of h can be expressed as a function of L as

$$(L/2\pi)\text{arctanh}(L/L_{t\infty}) \leq h \leq (L/2\pi)\text{arccosh}(L/AL_{t\infty}). \tag{2}$$

The ripple predictor

Diem's[14] central assumption is that the orbital diameter can be expressed in terms of an equilibrium ripple wavelength, λ_e, as

$$\lambda_e = \alpha_0 d_0, \tag{3}$$

where $\alpha_0 = 0.65$, based on the experiments[20], provided that $\lambda_e < 200$ mm ($d_0 = 308$ mm). Above this limit, Diem[14] used the Sleath[21] predictor. This arbitrary 200-mm limit represents the lower boundary of the suborbital and anorbital ranges, where the wavelength is dependent on both d_0 and D_{50} for suborbital ripples and only dependent on D_{50} for anorbital ripples. However, while a value of α_0 in the range $0.5 \leq \alpha_0 \leq 0.75$ in eq. (3) is widely accepted, there is little agreement in the literature on the precise nature of the orbital, suborbital, and anorbital limits[22]. Wiberg and Harris[3] defined orbital, suborbital and anorbital ripples by $d_0/D_{50} \leq 1754$, $1754 < d_0/D_{50} \leq 5587$ and $d_0/D_{50} > 5587$, respectively[23], whereas other researchers have argued the anorbital limit should have wave-period dependence[24,25]. Provided that eq. (3) *does* hold, which is what will be assumed here, all quantities involving d_0 can now be expressed in terms of λ_e.

Adaptions to the Diem[14] approach

Threshold of motion parameterisation

Based on the Soulsby[26] critical threshold of motion for clean sand, the methods section derives an expression for U_t^2, eq. (11), such that U_t^2, $L_{t\infty}$ and $AL_{t\infty}$ can be written

$$U_t^2 = B(g d_0^{0.52} D_{50}^{0.48}), \quad L_{t\infty} = \frac{\pi d_0}{2B}\left(\frac{d_0}{D_{50}}\right)^{0.48}, \quad AL_{t\infty} = \frac{d_0}{0.142}, \tag{4a,b,c}$$

where $B = 3.653(s-1)\theta_0$, s is the relative density of sediment in water, θ_0 is the critical skin friction Shields parameter, eq. (10), and $d_0 = \lambda_e/\alpha_0$ from eq. (3). Diem[14] used the Komar and Miller[27] mobility threshold prescription. Here, the Soulsby[26] expression has been used, as it allows U_t^2 to be directly related to θ_0 and it avoids the need for two different functional forms, for $D_{50} < 0.5$ mm and $D_{50} \geq 0.5$ mm (eqs. (12) and (13)).

Inclusion of the effect of clay

Wu et al.[13] showed that the ratio of wavelength to orbital diameter, α, which replaces α_0 in eq. (3), can be expressed as

$$\alpha = \alpha_0 \times \begin{cases} 1, & C_0 \leq C_{0m}, \\ 1 - 5.5(C_0 - C_{0m}), & C_0 > C_{0m}, \end{cases} \tag{5}$$

where α_0 is the clean-sand constant of proportionality (= 0.61), C_0 is the clay content in the bed, C_{0m} = 7.4% is the minimum value of C_0 where α can change from α_0 and $\alpha = \frac{1}{2}\alpha_0$ for $C_0 = 16.3\%$. Whitehouse et al.[28] showed that the threshold of motion is enhanced by the clay content according to

$$\theta_{0E} = \theta_0 B_\theta, \tag{6}$$

where θ_0 is the clean-sand threshold, $B_\theta = 1 + P_\theta C_0$ and P_θ is a constant that depends on the sediment properties. Based on their experiments, Wu et al.[13] determined that $P_\theta = 6.3$ for $D_{50} = 0.143$ mm and $P_\theta = 23$ for $0.45 \leq D_{50} \leq 0.5$ mm (between these two ranges, it will be assumed that P_θ can be linearly interpolated). Notice in eq. (6) that even small amounts of clay produce an enhancement which is strongly dependent on grain size.

Thus, the two main effects of including clay are that α is reduced and θ_{0E} is increased. Substituting eqs. (5) and (6), into eqs. (4a,b,c) gives U_t^2, $L_{t\infty}$ and $AL_{t\infty}$ as

$$U_t^2 = B\left[\frac{B_\theta}{\alpha^{0.52}}\right](g\lambda_e^{0.52} D_{50}^{0.48}), \quad L_{t\infty} = \frac{\pi\lambda_e}{2B[B_\theta \alpha^{1.48}]}\left(\frac{\lambda_e}{D_{50}}\right)^{0.48}, \quad AL_{t\infty} = \frac{\lambda_e}{0.142[\alpha]}, \tag{7a,b,c}$$

where λ_e is the mixed clay–sand ripple wavelength and only the square-bracketed quantity in each expression depends on C_0.

The adapted procedure

The procedure begins with the determination of the ripple wavelength, λ_e, and bed-clay content, C_0. Once these have been determined, the following calculations are undertaken:

(i) Use λ_e and C_0 in eqs. (7a,b,c), with α and B_θ given by eqs. (5) and (6), to determine U_t, $L_{t\infty}$ and $AL_{t\infty}$

(ii) Use A in eq. (9) to determine $x_{max,min}$, so that $x_{min} \le x \le x_{max}$

(iii) Use $L = L_{t\infty}x$ to determine the range of h based on eq. (2) and U_t and $U_m = (0.0355\pi g\lambda_e/\alpha)^{½}$ to determine the ranges of U_0 and T: $U_t < U_0 < U_m$ and $\pi\lambda_e/\alpha U_m < T < \pi\lambda_e/\alpha U_t$

Example cases

With specific examples from the rock record, Diem[14] was able to show how local considerations and context could be used to further limit the theoretical ranges described in the previous section. Here, modern-day examples, where the wave properties are known, are used, so that attention can be focussed on the effect of clay on the theoretical ranges alone. The example cases correspond to clean, coarse-, medium- and fine-grained sand from the laboratory and field, and involve determining how wave conditions based on the measured ripples change if the clay content is varied in the range $0 \le C_0 \le 16.3\%$.

Wu et al.[11], coarse-sand laboratory data

Wu et al.[11] conducted a series of experiments involving a single-wave condition over a bed composed of well-sorted coarse sand, $D_{50} = 0.496$ mm ($\theta_0 = 0.032$), and varying clay content, $0 \le C_0 \le 7.4\%$. For the clean sand experiment ($C_0 = 0\%$), the wave conditions were given by $h = 0.6$ m, $H = 0.16$ m and $T = 2.49$ s ($L = 5.62$ m), corresponding to $d_0 = 0.223$ m. This experiment produced ripples with a wavelength $\lambda_e = 278D_{50}$[13]. Figure 2a show the threshold and wave-breaking scales, $L_{t\infty}$ and $AL_{t\infty}$, versus C_0. $L_{t\infty}$, which is smallest at $C_0 = 7.4\%$, has a much larger range than $AL_{t\infty}$, which is constant for $C_0 \le 7.4\%$ and then doubles up to $C_0 = 16.3\%$. Figure 2d shows the corresponding L-h phase space, based on eq. (2), for the clay contents depicted in Figure 2a ($C_0 = 0$, 7.4 and 16.3%). Compared to the dimensionless x–kh plot (Figure 1), the threshold curves are still concave downwards, but more exaggerated, and the breaking-wave curves are close to straight lines. The change in ranges is largely due to changes in $L_{t\infty}$. The reduction in range between the largest and smallest (corresponding to C_0 = 0% and 7.4%) is by a factor of 3 and 4 for the water-surface wavelength and water depth, respectively (Figure 2d). Notice that the actual surface wavelength and water depth ($L = 5.62$ m, h = 0.6 m) are within all three ranges. Figures 2a,d can be compared with Figures 4a,b to see the effect of using the Komar and Miller[27] clean-sand mobility description for the threshold. This shows $L_{t\infty}$ to be about 63% of its value in Figure 2a, because $B = 0.21(s–1) = 0.34$ as opposed to $3.653(s–1)\theta_0$ = 0.19. Thus, using the Diem[14] clean-sand mobility description underpredicts the range of water-surface wavelengths and heights in an absolute sense. In a relative sense, the change in the ranges of clay content is similar, because the powers of d_0 and D_{50} are similar (eq. (13), for $D_{50} < 0.5$ mm, and eq. (7a)), but this will not be the case for $D_{50} > 0.5$ mm. Also, the measured L and h are not within the C_0 = 7.4% range (Figure 4b). As L and h are below the threshold curve, this would imply that ripples of this size are relict for this clay content. This is inconsistent with the experimental results, since Wu et al.[13] showed no reduction in λ_e for $C_0 \le 7.4\%$.

Doucette[29], medium-sand field data

The Doucette[29] field measurements were taken on a microtidal beach of Wambro Sound, Western Australia, near Perth (run 1) where $h = 0.47$ m, $H = 0.2$ m and $T = 5.6$ s ($L = 11.9$ m), corresponding to $d_0 = 0.79$ m. The bed was composed of medium sand, with $D_{50} = 0.22$ mm ($\theta_0 = 0.045$), and the measured ripples had a wavelength of $\lambda_e = 250$ mm. Since $d_0/D_{50} = 3591$, the ripples were in the suborbital range, where the wavelength is dependent on both the orbital and grain diameters. Notice this wavelength is above Diem's[14] 200-mm limit. The methods section demonstrates that, whilst using the Sleath[21] predictor for $C_0 = 0$ produces a difference, it is similar to the other two example cases, which are below the Diem[14] limit, and so is not considered significant. From interpolation, P_θ in eq.

(6) is determined to be 10. Figure 2b shows $L_{t\infty}$ and $AL_{t\infty}$ versus C_0 and Figure 2e shows the L–h phase space, for C_0 = 0, 7.4 and 16.3%. These reveal similar behaviour to that of the coarse-grained sand case, but less extreme: in Figure 2b, $L_{t\infty}$ is still at its minimum at C_0 = 7.4% and $AL_{t\infty}$ shows the same enhancement as in Figure 2a. The reduction in range between the largest and smallest (C_0 = 0% and 7.4%) is by a factor of 2 for both the water-surface wavelength and water depth (Figure 2e). Again, the actual surface wavelength and water depth (L = 11.9 m, h = 0.47 m) are within all three ranges.

Boyd et al.[30], fine-sand field data

The Boyd et al.[30] field measurements were undertaken about 1 km from Martinique Beach on the Atlantic coast of Nova Scotia during a period of relative calm (day 167, hour 9) where h = 10 m, H = 0.5 m and T = 6.2 s (L = 50.7 m), corresponding to d_0 = 0.32 m. The bed was composed of well-sorted fine sand, with D_{50} = 0.11 mm (θ_0 = 0.076), and the measured ripples had a wavelength of λ_e = 180 mm. d_0/D_{50} = 2873 puts the ripples into the suborbital range. Assuming that P_θ in eq. (6) is the same as for 0.143 mm (P_θ = 6.3), Figure 2c shows $L_{t\infty}$ and $AL_{t\infty}$ versus C_0 and Figure 2f shows the L–h phase space, for C_0 = 0, 7.4 and 16.3%. $L_{t\infty}$ in Figure 2c is still at its minimum at C_0 = 7.4%, but, because of far weaker clay enhancement of the threshold for fine sands in eq. (6), $L_{t\infty}$ is largest for C_0 = 16.3%. In Figure 2f, the measured water-surface wavelength and water depth (L = 50.7 m, h = 10 m) are below the threshold curve and outside the range for the C_0 = 0 and 7.4% clay contents, and just above the threshold curve and within range for C_0 = 16.3%, because, unlike the previous cases, C_0 = 16.3% produces the largest $L_{t\infty}$. Since there was little clay at the field site, the wave conditions were probably below threshold, implying that the observed ripples were relict. This is supported by the fact that Boyd et al.'s[30] previous observation at day 167, hour 3, showed the same wavelength and no ripple migration. The reduction in range between the largest and smallest (C_0 = 16.3% and 7.4%) is again by a factor of 2 for both the water-surface wavelength and water depth (Figure 2f).

Discussion

The range of L shown in Figure 2 is largely controlled by $L_{t\infty}$, so it is of interest to determine how the change in clay content affects $L_{t\infty}$, eq. (7b), compared to the original clean-sand Diem[14] method using Komar and Miller[27], $L_{t\infty KM}$, eq. (13) with C_0 = 0%. The net effect is shown as a ratio in Figure 3 for C_0 = 0, 7.4 and 16.3% and 0.1 ≤ D_{50} ≤ 0.8 mm, for the approximate limits in the range of λ_e/D_{50} of 250 and 1,000. There are two competing effects: the reduction because of clay content (Figure 2) and the increase because of using the Soulsby[26] threshold condition rather than the Komar and Miller[27]. Figure 3 shows a discontinuity for clean sand at D_{50} = 0.5 mm as a result of eq. (13), leading to the largest difference ($L_{t\infty}$ is increased by up to 161% for λ_e/D_{50} = 250), which decreases with increasing λ_e/D_{50} (although the Diem[14] method has rarely been applied for D_{50} > 0.5 mm). Otherwise for D_{50} ≤ 0.19 mm, $L_{t\infty}$ is reduced by up to 36%, and for 0.19 < D_{50} ≤ 0.5 mm, $L_{t\infty}$ is increased by up to 64%. For C_0 = 7.4%, $L_{t\infty}$ is consistently decreased by between 35 and 56%, and for C_0 = 16.3%, $L_{t\infty}$ varies only slightly (increased by up to 14%, for 0.12 ≤ D_{50} ≤ 0.37 mm, and otherwise reduced by up to 15%). The absence of a discontinuity in the present formulation, compared to Diem's[14] original formulation, is clearly preferable. Also, the net effect of the clay on $L_{t\infty}$ will be stronger for smaller than for larger clay contents.

It is important to clarify how a representative clay content, C_0, for the ripples should be determined. In the modern environment this usually involves measuring C_0 below the active layer (below trough level), as efficient winnowing often removes clay from the body of the ripples during development[12]. In the geological record, clay content in deposits should be based on primary clay minerals and diagenetic alterations for which it can be established that the original mineral was part of the primary clay fraction.

Conclusions

Preserved sedimentary bedforms provide important information for reconstructing past hydraulics in subaqueous environments by inverting bedform predictors, but this is usually based exclusively on non-cohesive sand. The present work incorporates the effects of sand-clay mixtures on bedforms, using the experimental results of Wu et al.[13] in the non-cohesive inversion method of Diem[14]. Based

on wave breaking and threshold of motion limitations, the Diem[14] approach results in ranges for wave conditions. Here we have shown that the inclusion of as little as 7.4% clay in the most extreme case of coarse sand, $D_{50} \geq 0.45$ mm, reduces the possible ranges of water-surface wavelengths and water depths by factors of 3 and 4, respectively. For fine sand, the ranges are reduced by a factor of two. In short, not accounting for the modifying effect of clay in ripple growth and equilibrium geometries, may lead to underestimating the prevailing flow conditions if clay is present.

Methods

Derivation of the Diem[14] approach

For linear wave theory, the dispersion relation and the wave-velocity amplitude, U_0, are

$$\sigma^2 = gk\tanh kh, \quad U_0 = \pi d_0/T, \tag{8a,b}$$

where $\sigma = 2\pi/T$, $d_0 = H/\sinh kh$ and $k = 2\pi/L$. The wave properties, characterised by eqs. (8a,b), are subject to two constraints: threshold of motion and wave breaking. For sediment movement $U_0^2 > U_t^2$, where U_t is the threshold wave-velocity amplitude to be determined below, which when combined with eqs. (8a,b) gives $x < \tanh kh$, eq. (1a), where $x = L/L_{t\infty}$ and $L_{t\infty} = \frac{1}{2}\pi g(d_0/U_t)^2$. The wave-breaking criterion[31] defines the maximum possible wave steepness as, $H/L \leq 0.142\tanh kh$, which when combined with d_0 and $L_{t\infty}$ gives $x \geq A\cosh kh$, eq. (1b), where $A = d_0/0.142L_{t\infty}$. It will be shown below, that $A < \frac{1}{2}$, so if $A = \frac{1}{2}(U_t/U_m)^2$, where $U_m = (0.0355\pi g d_0)^{1/2}$ is the maximum wave-velocity amplitude ($U_m > U_t$), then $U_t < U_0 \leq U_m$ and from eq. (8b) $\pi d_0/U_m \leq T < \pi d_0/U_t$.

The limits of the possible values of x can be found by combining eqs. (1a,b) using the identity $1-\tanh^2 kh = \operatorname{sech}^2 kh$, such that the maximum and minimum in x satisfy the equation $x^4 - x^2 + A^2 = 0$, so that $x_{max,min}$ are

$$x_{max,min} = [\tfrac{1}{2} \pm \tfrac{1}{2}(1 - 4A^2)^{1/2}]^{1/2}, \tag{9}$$

where $A < \frac{1}{2}$, for there to be two distinct values. Here, x and kh are in the ranges $x_{min} \leq x < x_{max}$ and $\operatorname{arctanh} x < kh \leq \operatorname{arccosh}(x/A)$, respectively. In Figure 1, for the limiting $A = \frac{1}{2}$ ($U_m^2 = U_t^2$) single-valued case the dot corresponds to $x = 2^{-1/2}$, from eq. (9), and $kh = \operatorname{arctanh} 2^{-1/2} \sim 0.88$. Likewise, in the $A = \frac{1}{4}$ ($U_m^2 = 2U_t^2$) case the dots mark $x_{max,min} = \frac{1}{2}(2 \pm 3^{1/2})^{1/2} \sim 0.97$, 0.26 and $kh_{max,min} = \operatorname{arctanh}(x_{max,min})$.

Determination of U_t^2 based on Soulsby[26]

According to Soulsby[26], the Shields parameter for the critical threshold of motion of clean sand is

$$\theta_0 = \frac{0.3}{1+1.2D_*} + 0.055(1-e^{-0.02D_*}), \tag{10}$$

where $D_* = [(s-1)g/\nu^2]^{1/3} D_{50}$, $s = \rho_s/\rho$, ρ_s and ρ are the water and sediment densities and ν is the kinematic viscosity (~ 1 mm^2 s^{-1}). For waves, $\theta_0 = f_w U_t^2/2(s-1)gD_{50}$, where $f_w = 1.39(6d_0/D_{50})^{-0.52}$ is the skin friction factor[32]. Rearranging the θ_0 wave expression gives U_t^2 as

$$U_t^2 = B(g d_0^{0.52} D_{50}^{0.48}), \tag{11}$$

where $B = 6^{0.52}(s-1)\theta_0/0.695 = 3.653(s-1)\theta_0$. Eq. (11) can be compared with eq. (12).

Diem[14] threshold of motion constraint

Diem[14] used the Komar & Miller[27] expression for U_t^2, namely

$$U_t^2 = (s-1)gd_0 \times \begin{cases} 0.21(d_0/D_{50})^{-0.5}, & D_{50} < 0.5 \text{ mm}, \\ 0.46\pi(d_0/D_{50})^{-0.75}, & D_{50} \geq 0.5 \text{ mm}, \end{cases} \tag{12}$$

such that with the inclusion of clay $L_{t\infty} = \pi g d_0^2/2B_\theta U_t^2$, $d_0 = \lambda_e/\alpha$ and B_θ and α are given by eqs. (5) and (6), giving $L_{t\infty}$ as

$$L_{t\infty} = \frac{\pi\lambda_e}{2(s-1)} \times \begin{cases} \dfrac{1}{0.21[B_0\alpha^{1.5}]}\left(\dfrac{\lambda_e}{D_{50}}\right)^{0.5}, & D_{50} < 0.5 \text{ mm}, \\ \dfrac{1}{0.46\pi[B_0\alpha^{1.75}]}\left(\dfrac{\lambda_e}{D_{50}}\right)^{0.75}, & D_{50} \geq 0.5 \text{ mm}, \end{cases} \tag{13}$$

and $AL_{t\infty}$ as $\lambda_e/0.142[\alpha]$ remains the same. Figure 4 shows the effect of this parameterisation of the threshold of motion for the first example case of Wu et al.[11] depicted in Figures 2a,d. Unlike Figure 2d, the measured values of h and L are outside the range predicted for $C_0 = 7.4\%$.

Using the Sleath[21] expression to predict d_0/λ_e

This section considers the effect of using the Sleath[21] expression for d_0/λ_e when $\lambda_e \geq 200$ mm and applies it to the three examples considered in the results section for the clean-sand case. In the clean-sand case, according to Diem[14], d_0/λ_e can be expressed as

$$\frac{d_0}{\lambda_e} = \begin{cases} \alpha_0^{-1}, & \lambda_e < 200 \text{ mm}, \\ 0.778R_s^{0.151}, & \lambda_e \geq 200 \text{ mm}, \end{cases} \tag{14}$$

where α_0 was taken to be 0.65, but here is 0.61, see eq. (6), and $R_s = (U_0 d_0/2\nu)^{½}$. If $\lambda_e < 200$ mm, then $\alpha_0^{-1}\lambda_e$ can be substituted for d_0, as explained in the main paper. However, for $\lambda_e \geq 200$ mm, since the d_0/λ_e ratio can change, Diem[14] showed that an additional step in the calculation was required. The wave-velocity amplitude must still be in the range $U_t < U_0 \leq U_m$, so that R_s is in the range $(U_t d_0/2\nu)^{½} < R_s \leq (U_m d_0/2\nu)^{½}$, and therefore from eq. (14), for $\lambda_e \geq 200$ mm, d_0/λ_e must be in the range $0.778(U_t d_0/2\nu)^{0.0755} < d_0/\lambda_e \leq 0.778(U_m d_0/2\nu)^{0.0755}$. From eq. (11), $U_t = (Bg)^{0.5} d_0^{0.26} D_{50}^{0.24}$, where $B = 3.653(s-1)\theta_0$, and $U_m = (0.0355\pi g d_0)^{0.5}$, so that the d_0/λ_e range is

$$P_1\left(\frac{g^{0.5}d_0^{1.26}D_{50}^{0.24}}{\nu}\right)^{0.0755} < \frac{d_0}{\lambda_e} \leq P_2\left(\frac{gd_0^3}{\nu^2}\right)^{0.03775}, \tag{15}$$

where $P_1 = 0.778(B/4)^{0.03775}$, $P_2 = 0.778(0.0355\pi/4)^{0.03775}$, and the minimum and maximum in the d_0/λ_e range correspond to the threshold of motion and wave breaking, respectively. For a given measured λ_e, the solution to eq. (15) requires an iteration starting from $d_0 = \alpha_0^{-1}\lambda_e = 1.64\lambda_e$. Substituting $\lambda_e(d_0/\lambda_e)_{min}$ and $\lambda_e(d_0/\lambda_e)_{max}$, from eq. (15), into eqs. (4a,b,c) allows the threshold of motion and wave breaking scales, $L_{t\infty}$ and $AL_{t\infty}$, to be expressed as

$$L_{t\infty} = \frac{\pi\lambda_e(d_0/\lambda_e)_{min}^{1.48}}{2B}\left(\frac{\lambda_e}{D_{50}}\right)^{0.48}, \quad AL_{t\infty} = \frac{\lambda_e(d_0/\lambda_e)_{max}}{0.142}. \tag{16a,b}$$

For each of the three example cases considered in the results section, $(d_0/\lambda_e)_{min}$ and $(d_0/\lambda_e)_{max}$ are listed in table 1, even though the $\lambda_e \geq 200$ mm condition is only met in the Doucette[29] case. In all three example cases, $d_0/\lambda_e = 1.64$ lies between $(d_0/\lambda_e)_{min}$ and $(d_0/\lambda_e)_{max}$. The observed and predicted d_0/λ_e are in close agreement, apart from the Doucette[29] case, where both the d_0/λ_e range from eq. (15) and $d_0/\lambda_e = 1.64$ underpredict by approximately a factor of two. The values of $L_{t\infty R}$ and $AL_{t\infty R}$ from eqs. (16a,b) and (4b,c) are also given in table 1. Since these values for $L_{t\infty R}$ and $AL_{t\infty R}$ are largely similar in all three cases, this suggests that using the orbital approximation $d_0/\lambda_e = 1.64$ for the Doucette[29] case is reasonable, even though $\lambda_e \geq 200$ mm.

Data	D_{50} mm	λ_e mm	d_0/λ_e -	θ_0 -	$(d_0/\lambda_e)_{min}$ -	$(d_0/\lambda_e)_{max}$ -	$L_{t\infty R}$ -	$AL_{t\infty R}$ -
Wu et al.[11]	0.496	138	1.64	0.032	1.04	1.79	0.51	1.09
Doucette[29]	0.22	250	3.16	0.045	1.07	1.94	0.53	1.18
Boyd et al.[30]	0.11	180	1.74	0.076	1.07	1.86	0.53	1.13

Table 1 Measured D_{50}, λ_e and d_0/λ_e and predicted θ_0 from eq. (10), $(d_0/\lambda_e)_{min}$ and $(d_0/\lambda_e)_{max}$ from eq. (15), $L_{t\infty R} = [0.61(d_0/\lambda_e)_{min}]^{1.48}$ and $AL_{t\infty R} = 0.61(d_0/\lambda_e)_{max}$, based on eqs. (16a,b) and (4b,c) for the three example cases.

Data availability

Eqs. (5) and (6) are from Wu et al.[13], which has its own open-access policy. For the three example cases, no other data outside that which is stated in the text and obtained from the references concerned[11,29,30] has been used in this paper.

References

1. Collinson, J. & Mountney, N. *Sedimentary structures* (Fourth Edition), Edinburgh, UK: Dunedin Academic Press (2019). ISBN 1780460627
2. Vignaga, E., Sloan, D.M., Luo, X., Haynes, H., Phoenix, V.R. & Sloan, W.T. Erosion of biofilm-bound fluvial sediments. *Nature Geoscience*, **6**, 770–774 (2013). doi: 10.1038/ngeo1891
3. Wiberg, P.L. & Harris, C.K. Ripple geometry in wave-dominated environments. *Journal of Geophysical Research*, **99**(C1), 775–789 (1994). doi: 10.1029/93JC02726
4. Baas, J.H. A flume study on the development and equilibrium morphology of current ripples in very fine sand. *Sedimentology*, **41**, 185–209 (1994). doi: 10.1111/j.1365-3091.1994.tb01400.x
5. Perron, J.T., Myrow, P.M., Huppert, K.L., Koss, A.R. & Wickert, A.D. Ancient record of changing flows from wave ripple defects. *Geology*, **46**, 875–878 (2018). doi: 10.1130/G45463.1
6. Cuadrado, D.G. Geobiological model of ripple genesis and preservation in a heterolithic sedimentary sequence for a supratidal area. *Sedimentology*, **67**, 2747–2763 (2020). doi: 10.1111/sed.12718
7. Allen, P.A. Some guidelines in reconstructing ancient sea conditions from wave ripplemarks. *Marine Geology*, **43**, 59–67 (1981). doi: 10.1016/0025-3227(81)90176-6
8. Davies, N.S., Liu, A.G., Gibling, M.R. & Miller, R.F. Resolving MISS conceptions and misconceptions: A geological approach to sedimentary surface textures generated by microbial and abiotic processes. *Earth-Science Reviews*, **154**, 210–246 (2016). doi: 10.1016/j.earscirev.2016.01.005
9. Malarkey, J., Baas, J.H., Hope, J.A., Aspden, R.J., Parsons, D.R., Peakall, J., Paterson, D.M., Schindler, R.J., Ye, L., Lichtman, I.D., Bass, S.J., Davies, A.G., Manning, A.J. & Thorne, P.D. The pervasive role of biological cohesion in bedform development. *Nature Communications*, **6**, 6257 (2015). doi: 10.1038/ncomms7257
10. Parsons, D.R., Schindler, R.J., Hope, J.A., Malarkey, J., Baas, J.H., Peakall, J., Manning, A.J., Ye, L., Simmons, S., Paterson, D.M., Aspden, R.J., Bass, S.J., Davies, A.G., Lichtman, I.D. & Thorne, P.D. The role of biophysical cohesion on subaqueous bed form size. *Geophysical Research Letters*, **43**, 1566–1573 (2016). doi: 10.1002/2016GL067667
11. Wu, X., Baas, J.H., Parsons, D.R., Eggenhuisen, J., Amoudry, L., Cartigny, M., McLelland, S., Mouazé, D. & Ruessink, G. Wave ripple development on mixed clay–sand substrates: Effects of clay winnowing and armoring. *Journal of Geophysical Research: Earth Surface*, **123**, 2784–2801 (2018). doi: 10.1029/2018JF004681
12. Wu, X., Fernández, R., Baas, J.H., Malarkey, J. & Parsons, D.R. Discontinuity in equilibrium wave–current ripple size and shape and deep cleaning associated with cohesive sand–clay beds. *Journal of Geophysical Research: Earth Surface*, **127**, e2022JF006771 (2022). doi: 10.1029/2022JF006771
13. Wu, X., Malarkey, J., Fernández, R., Baas, J.H., Pollard, E. & Parsons, D.R. Influence of cohesive clay on wave-current ripple dynamics captured in a 3D phase diagram. *Earth Surface Dynamics*, **12**, 231–247 (2024). doi: 10.5194/esurf-12-231-2024
14. Diem, B. Analytical method for estimating palaeowave climate and water depth from wave ripple marks. *Sedimentology*, **32**, 705–720 (1985). doi: 10.1111/j.1365-3091.1985.tb00483.x
15. Aspler, L.B., Chiarenzelli, J.R. & Bursey, T.L. Ripple marks in quartz arenites of the Hurwitz group, Northwest territories, Canada: evidence for sedimentation in a vast, early Proterozoic, shallow, fresh-water lake. *Journal of Sedimentary Research*, **A64**, 282–298 (1994). doi: 10.1306/D4267D7F-2B26-11D7-8648000102C1865D
16. Wetzel, A., Allenbach, R. & Allia, V. Reactivated basement structures affecting the sedimentary facies in a tectonically “quiescent” epicontinental basin: an example from NW Switzerland. *Sedimentary Geology*, **157**, 153–172 (2003). doi: 10.1016/S0037-0738(02)00230-0

17. Allen, P.A. & Hoffman, P.F. Extreme winds and waves in the aftermath of a Neoproterozoic glaciation. *Nature*, **433**, 123–127 (2005). doi: 10.1038/nature03176
18. Pochat, S. & Van Den Driessche, J. Filling sequence in Late Paleozoic continental basins: A chimera of climate change? A new light shed given by the Graissessac–Lodève basin (SE France). *Palaeogeography, Palaeoclimatology, Palaeoecology*, **302**, 170–186 (2011). doi: 10.1016/j.palaeo.2011.01.006
19. Lamb, M.P., Fischer, W.W., Raub, T.D., Perron, J.T. & Myrow, P.M. Origin of giant wave ripples in snowball Earth cap carbonate. *Geology*, **40**, 827–830 (2012). doi: 10.1130/G33093.1
20. Miller, M.C. & Komar, P.D. Oscillation sand ripples generated by laboratory apparatus. *Journal of Sedimentary Petrology*, **50**, 173–182 (1980). doi: 10.1306/212F799B-2B24-11D7-8648000102C1865D
21. Sleath, J.F.A. A contribution to the study of vortex ripples. *Journal of Hydraulic Research*, **13**, 315–328 (1975). doi: 10.1080/00221687509499705
22. Vittori, G. & Blondeaux, P. On the prediction of the characteristics of sand ripples at the bottom of sea waves. *Earth-Science Reviews*, **252**, 104753 (2024). doi: 10.1016/j.earscirev.2024.104753
23. Malarkey, J. & Davies, A.G. A non-iterative procedure for the Wiberg and Harris (1994) oscillatory sand ripple predictor. *Journal of Coastal Research*, **19**, 738-739 (2003).
24. Mogridge, G.R., Davies, M.H. & Willis, D.H. Geometry prediction for wave-generated bedforms. *Coastal Engineering*, **22**, 255–286 (1994). doi: 10.1016/0378-3839(94)90039-6
25. Pedocchi, F. & García, M.H. Ripple morphology under oscillatory flow: 2. Experiments. *Journal of Geophysical Research*, **114**, C12015 (2009). doi: 10.1029/2009JC005356
26. Soulsby, R. *Dynamics of Marine Sands: A Manual for Practical Applications*, London UK: Thomas Telford (1997). ISBN 072772584X
27. Komar, P.D. & Miller, M.C. The threshold of sediment movement under oscillatory water waves. *Journal of Sedimentary Petrology*, **43**, 1101–1110 (1973). doi: 10.1306/74D7290A-2B21-11D7-8648000102C1865D
28. Whitehouse, R., Soulsby, R., Roberts W. & Mitchener, H. *Dynamics of estuarine muds: A Manual for Practical Applications*, London UK: Thomas Telford (2000). ISBN 0727728644
29. Doucette, J.S. The distribution of nearshore bedforms and effects on sand suspension on low-energy, micro-tidal beaches in Southwestern Australia. *Marine Geology*, **165**, 41–61 (2000). doi: 10.1016/S0025-3227(00)00002-5
30. Boyd, R., Forbes, D.L. & Heffler, D.E. Time-sequence observations of wave-formed sand ripples on an ocean shoreface. *Sedimentology*, **35**, 449–464 (1988). doi: 10.1111/j.1365-3091.1988.tb00997.x
31. Miche, R. Mouvements ondulatoires de la mer en profondeur constante ou décroissante. *Annales des Ponts et Chaussées*, **19**, 369–406 (1944).
32. Soulsby, R.L., Hamm, L., Klopman, G., Myrhaug, D., Simons, R.R. & Thomas, G.P. Wave–current interactions within and outside the bottom boundary layer. *Coastal Engineering*, **21**, 41–69 (1993). doi: 10.1016/0378-3839(93)90045-A

Acknowledgments

The participation of JM, EMP, XW, RF, JHB and DRP was made possible thanks to funding by the European Research Council under the European Union's Horizon 2020 research and innovation program (grant no. 725955). Participation of RF was also supported by the Leverhulme Trust, Leverhulme Early Career Researcher Fellowship (grant ECF-2020-679).

Author Contributions

EMP and RF came up with the concept, based on the experiments undertaken by XW and RF, with assistance from JM in the synthesis. DRP provided the funding for the experiments. JM undertook the analysis and wrote the paper with input from all authors.

Competing interests

The authors declare no competing interests.

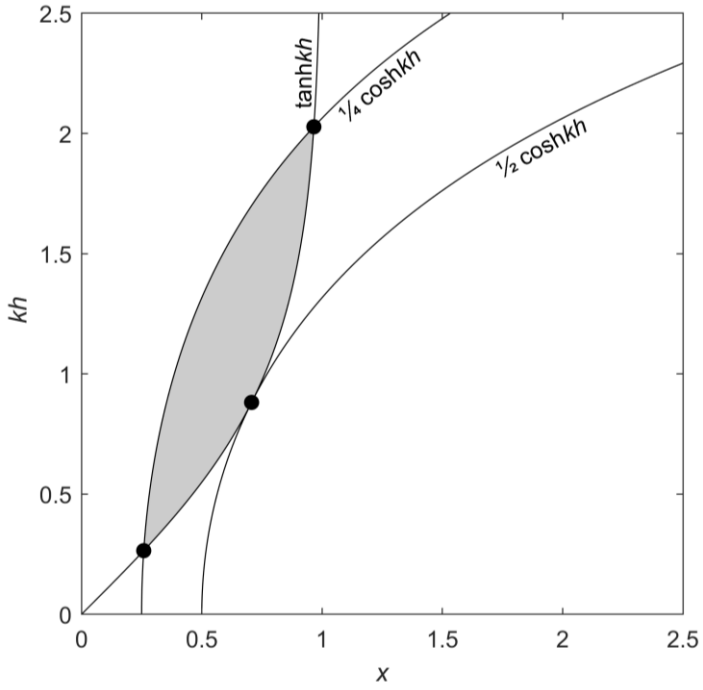

Figure 1 kh versus x ($L/L_{t\infty}$) for the limiting case of A = ½ and also A = ¼. The dots correspond to x = $2^{-½}$ and kh = arctanh$2^{-½}$, for A = ½; $x_{max,min}$ = ½$(2\pm3^{½})^{½}$ and $kh_{max,min}$ = arctanh[$x_{max,min}$], for A = ¼ (see methods, eq. (9)), and shading represents allowable values of x and kh for A = ¼ (¼cosh$kh \leq x \leq$ tanhkh).

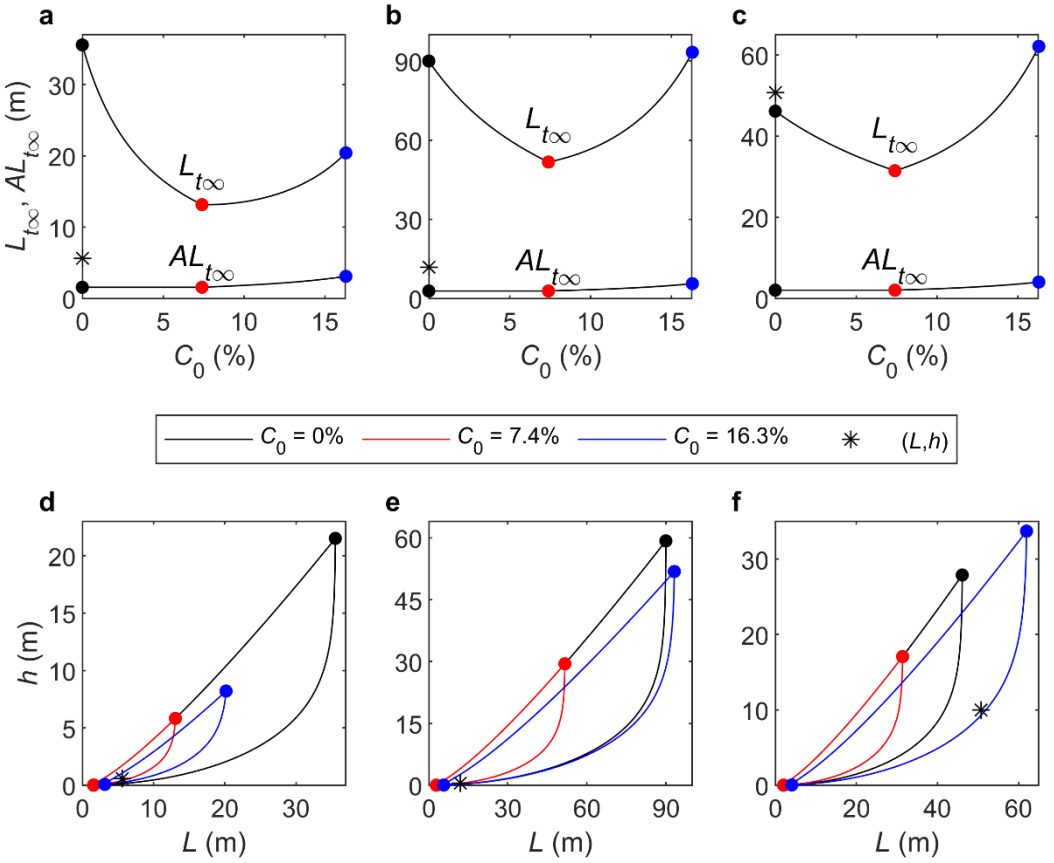

Figure 2 (a,b,c) Threshold, $L_{t\infty}$, and wave-breaking, $AL_{t\infty}$, scales, eqs. (7b,c), versus C_0 and (d,e,f) L–h phase space from eq. (2), showing the different ranges for C_0 = 0, 7.4 and 16.3% and the measured L and h. For (a,d) Wu et al.[11], $\lambda_e = 278D_{50}$, D_{50} = 0.496 mm, θ_0 = 0.032, L = 5.62 m and h = 0.6 m; for (b,e) Doucette[29], λ_e = 250 mm, D_{50} = 0.22 mm, θ_0 = 0.045, L = 11.9 m and h = 0.47 m, and for (c,f) Boyd et al.[30], λ_e = 180 mm, D_{50} = 0.11 mm, θ_0 = 0.076, L = 50.7 m and h = 10 m. Legend applies to d,e,f; colours in a,b,c are consistent with the legend.

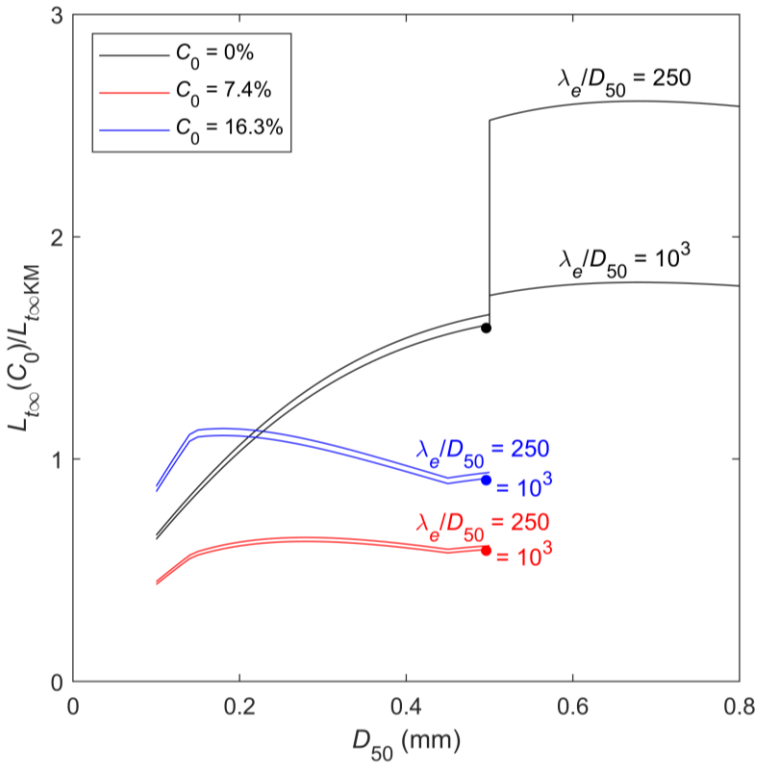

389 **Figure 3** Relative size of $L_{t\infty}(C_0)$ from eq. (7b) normalised by the clean-sand $L_{t\infty}$ from eq. (13), $L_{t\infty KM}$,
390 for C_0 = 0, 7.4 and 16.3%. λ_e/D_{50} = 250 and 1000, and the dots correspond to the Wu et al.[11] clean-
391 sand experiment in Figure 2a.

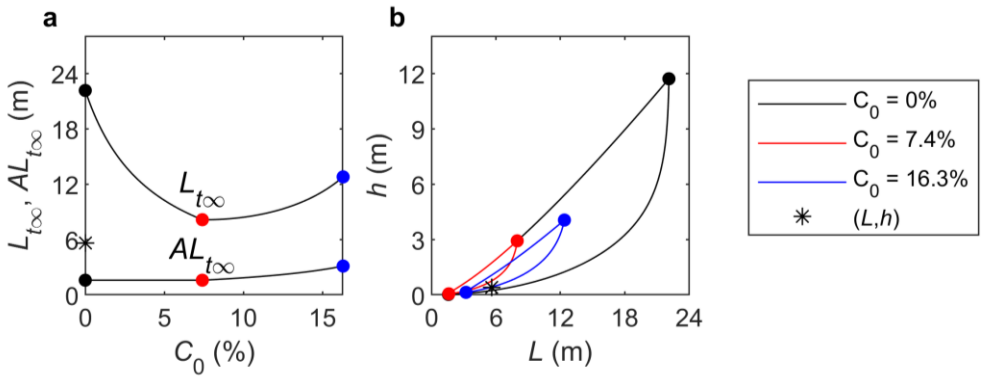

392 **Figure 4** (a) Threshold, $L_{t\infty}$, and wave-breaking scales, $AL_{t\infty}$, eqs. (13) and (7c), versus C_0 and (b) L–
393 h phase space from eq. (2) showing the different ranges for C_0 = 0, 7.4 and 16.3% and the measured
394 h and L for Wu et al.[11], $\lambda_e = 278D_{50}$, D_{50} = 0.496 mm, h = 0.6 m and L = 5.62 m.